Untargeted Metabolite Mapping in 3D Cell Culture Models using High Spectral Resolution FT-ICR Mass Spectrometry Imaging

Untargeted Metabolite Mapping in 3D Cell Culture Models using High Spectral Resolution FT-ICR Mass Spectrometry Imaging

Lulu H. Tucker[1] Gregory R. Hamm[2] Rebecca J. E. Sargeant[2] Richard J. A. Goodwin[2] C. Logan Mackay[1] Colin J. Campbell[1]* David J. Clarke[1]*

1 EaStCHEM School of Chemistry, University of Edinburgh, UK EH9 3FJ

2 Pathology, Clinical Pharmacology & Safety Sciences, BioPharmaceuticals R&D, AstraZeneca, CB4 0WG, UK

Keywords: Mass Spectrometry Imaging, Matrix-assisted laser desorption/ionization, spheroids, 3D cell culture

ABSTRACT: Multicellular tumor spheroids (MTS) are a well-established model system for drug development and are a valuable in vitro research tool for use prior to employing animal models. These 3D-cell cultures are thought to display chemical gradients of oxygen and nutrients throughout their structure, giving rise to distinct microenvironments in radial layers, thus mimicking the pathophysiological environment of a tumor. Little is known about the localized distributions of metabolites within these microenvironments. To address this, here we utilize high spectral resolution Fourier-transform ion cyclotron resonance (FT-ICR), MALDI mass spectrometry imaging (MSI) to image the distribution of endogenous metabolites in breast cancer MCF-7 spheroids. We show that known specific metabolite markers (adenosine phosphates and glutathione) indicate that the central region of these cell culture models experiences increased hypoxic and oxidative stress. By using discriminatory analysis, we have identified which *m/z* values localize towards the outer proliferative or central hypoxic regions of an MTS and have assigned elemental formula with sub-ppm error. Using this information, we have mapped these metabolites back to distinct pathways to improve our understanding of the molecular environment and biochemistry of these tumor models.

Introduction

Conventionally, adherent mammalian cells are cultured in monolayers under carefully controlled conditions to produce a homogenous population that offers simple and effective experimental consistency.[1] These 2-dimensional (2D) cell cultures are indispensable model systems utilized in a wide range of basic and clinical in *vitro* studies. However, despite its widespread use, 2D cell culture fails to capture the multifaceted physiology of the in *vivo* tissue microenvironment, which is composed of numerous complex structures and intricate relationships.[2] 3-dimensional (3D) cell culture combines the experimental simplicity of monolayer culture whilst retaining many of the complex morphological structures of a tissue.[3] Multicellular tumor spheroids (MTS) are spherical self-assembled aggregates that, above a critical size, display gradients of oxygen, nutrients and metabolite waste similar to those found in tumors. Thus, mature MTS display a zoned structure containing a central hypoxic region, surrounded by a layer of quiescent cells and an outer rim of rapidly proliferating cells.[4,5]

A number of analytical techniques have been used to elucidate the biology of these structures, such as Raman spectroscopy;[6] as well as several proteomic studies - including 2D polyacrylamide gel electrophoresis (PAGE)[7] followed by liquid chromatography mass spectrometry (LC-MS),[8] and stable isotope labelling of amino acids in cell culture (SILAC).[9] However, these analyses often rely on bulk assays on large numbers of MTS and thus disregard any heterogeneity present within spheroids. Therefore, the capacity to study a single MTS enables the identification of spatial variation within a spheroid caused by zonation.[8] Single spheroid studies are possible through serial trypsinization and subsequent MS of each spheroid layer,[10] and imaging techniques such as confocal Raman microscopy[11] and mass spectrometry imaging (MSI),[5] which offer the potential to observe spatial distributions of molecules that play an important role in cancer metabolism. Extensive sample preparation and handling affects the composition and detection of metabolites; so MSI offers the advantage of capturing the metabolite distributions with minimal sample processing.[12–14]

Matrix-assisted laser desorption/ionization (MALDI) MSI combines the principles of conventional MALDI-MS with spatial resolution, enabling broad spectral and label-free analysis to discern the distribution of ionizable compounds without requiring significant preceding knowledge.[12,15–17] MSI was first applied to study MTS in 2011 to observe the distribution of proteins within individual human carcinoma (HCT 116) spheroids.[5] Li and co-workers found that cytochrome C and histone H4 distributed uniformly across the spheroid and confirmed the identities of these proteins with nanoLC-MS/MS. Since this first report, several other studies have applied MSI to investigate MTS in a spatially-resolved manner. These include observing the distribution of lipids,[18] and the time-dependent penetration of drugs.[10,19–21]

However, despite the recent advances in MSI of spheroids, the majority of the work has been carried out using time-of-flight (ToF) MS.[22] Whilst ToF-MS instruments provide high sensitivity and relatively fast acquisition of MSI data, they typically have a mass resolving power up to 50,000.[23] As a result, these instruments lack the resolving power and mass accuracy required for definitive determination of elemental formula from accurate *m/z* measurements. In contrast, the high mass resolution and accuracy of Fourier-transform ion cyclotron resonance (FT-ICR) MS enables confident assignment of elemental formula,[24] and FT-ICR MS is widely used for characterization of unknown metabolites.[25,26] In an imaging workflow, FT-ICR MS enables the simultaneous distribution of known metabolites to be visualized without employing MS/MS techniques.[27]

Here, we combine the high spectral resolution available using the 12T FT-ICR (Bruker, Bremen, Germany) with spatial resolution imaging at 50 µm for the untargeted analysis of metabolites within MCF-7 spheroids. We show that metabolite markers indicate regions of increased hypoxia and oxidative stress within spheroids and we use discriminatory analysis to identify metabolites that colocalize to these areas. Finally, we demonstrate that this approach can be used to investigate the regional flux through specific biochemical pathways.

Materials and Methods

Cell culture and spheroids preparation. MCF-7 cells were donated at passage 52 from the Queen's Medical Research Institute (QMRI), Edinburgh (UK). Both monolayer cells and spheroids were grown in Dulbecco's Modified Eagles Medium (DMEM) (Thermo-Fisher, Massachusetts, USA) supplemented with 10% fetal calf serum (FCS) (Sigma Aldrich, Missouri, USA) and 1% penicillin (Thermo-Fisher, Massachusetts, USA). Monolayer cells were routinely seeded every 4 days in 75 cm^3 flasks with 1 mL cells and 9 mL fresh media. The media was replaced every 48 hours.

Spheroids were obtained using the hanging drop method.[6] Approximately 6000 cells were seeded into 20 µL droplets that were then suspended from the lid of a petri dish. A reservoir of 10 mL media was placed in the bottom of the dish. Spheroids were fed with 5 µL fresh media every 48 hours. Spheroids were incubated at 36.5 °C, 5% CO_2 and 95% humidity for 8 days before imaging.

MALDI imaging sample preparation

Preparation of spheroids. 8-day-old untreated MCF-7 spheroids were prepared using the following method. Media was removed, and spheroids were washed with ammonium formate (20 µL, 50 mM). Each spheroid was picked up using a 20 µL pipette and placed into a droplet from which the maximum amount of liquid was removed. To aid spheroid detection during sectioning, blue dyed gelatin (40 µL, 10% w/v) was placed onto the spheroids and frozen on isopentane and dry ice (2 minutes). The gelatin blocks were then snap frozen in liquid nitrogen and stored (-80 °C) until sectioning. Sectioning was performed using a Leica CM 1900 cryostat at -21 ºC (Leica Biosystems, Nussloch, Germany). Sections (15 µm) were cut and thaw mounted onto conductive indium tin-oxide (ITO)-coated glass slides (Bruker Daltonics, Bremen, Germany). Consecutive sections were taken for haematoxylin and eosin (H&E) staining. An optimized converted 3D printer[28] was used to apply 8 coats of 9-aminoacridine (9AA) matrix (10 mg/mL, 70% ACN), at a flow rate of 0.1 mL/minute at 40 °C with a gas pressure of 50 psi, a z height of 30 mm and velocity of 1100 mm/minute. These parameters resulted in a matrix density of 0.11 mg/cm^2.

H&E Staining. Sectioned spheroids were placed onto a glass slide and stored in a vacuum desiccator (room temperature, 18h). Sections were covered with haematoxylin (Sigma-Aldrich, Missouri, USA) (3 minutes) and washed with running water. The slide was coated with tap water (1 minute), then acid alcohol (Sigma-Aldrich, Missouri, USA) (20 seconds) and then washed using water. Eosin (Sigma-Aldrich, Missouri, USA) was added (1 minute) and then washed with water. The stained cells were then air dried before being imaged under the 40x objective on an inverted AE2000 (Motic, Hong Kong) microscope. Experiments were repeated for six biological replicates.

MALDI Mass Spectrometry Imaging. For this study, all mass spectrometry experiments were performed on a 12T SolariX FT-ICR MS equipped with an infinity ICR cell and a MALDI ionization using a SmartBeam II UV laser (Bruker Daltonics, Bremen, Germany) in negative ion mode using 9AA matrix. An *m/z* range of 98-1500 was acquired in broadband mode with a data acquisition time per pixel of 2 MWord. The laser raster increment was set to 40 µm along both the *x* and *y* axis with a smart walk of 50 µm. Laser focus was set to minimum (15 µm), with a frequency of 1000 Hz. Ions were accumulated across 300 laser shots for each mass analysis. Calibration of the spheroid data was performed post-processing by exporting pixels from FlexImaging 4.1 into DataAnalysis 4.4 and calibrated using a pre-determined list of internal calibrants (supporting information Table S1). The images were then analyzed with total ion count (TIC) normalization using SCiLS software version 2019a (Bruker Daltonics, Bremen, Germany). Ion maps were generated with a semiquantitative color scale bar normalized to the TIC. The mass resolution at *m/z* 300 was *ca.* 100000.

Discriminatory analysis. The spheroids were segregated into the 'outer' and 'central' regions based on 50% of the radius. For automatically finding *m/z* values discriminating the outer and central regions, the receiver operating characteristic (ROC) tool was employed and the area under the ROC curve (AUC value) was calculated (SCiLS, Bruker Daltonics). A threshold was set for the top five discriminatory *m/z* values. Using a representative pixel from either region, the calibrated *m/z* values were then assigned formulae using Human Metabolome Database (HMDB) http://www.hmdb.ca/spectra/ms/search with an error tolerance of 1 ppm for the $[M-H]^-$ ion. The distributions of identified discriminatory metabolites were verified manually with at least six biological replicates. For comparison of the ion abundances of individual species between regions of spheroids, ion abundance distributions were represented as box and whisker plots using SCiLS software.

Results and Discussion

Cell culture and spheroids preparation. This study was performed with MCF-7 3D cell cultures grown over 8 days to form spheroids of approximately 500 µm in diameter. To prepare the samples, the spheroids were embedded in gelatin and sections were taken close to the hemisphere of individual spheroids. Before MS analysis, H&E staining was used to confirm the structural integrity of the sections (see Figure 1A and supporting information Figure S1). Spheroid sections were then coated in matrix and subject to MALDI FT-ICR MS.

Initial high mass resolution MSI analysis across MTS. When MTS are grown to diameters above 200 µm, they are known to display gradients of oxygen, nutrients and waste products, producing a hypoxic environment in the central core.[6] In order to visualize the distribution of metabolites across these gradients, we employed a MALDI MSI workflow with high resolution FT-ICR MS. Spheroid sections were imaged in negative-ion mode using 9AA matrix at 50 µm spatial resolution between *m/z* 98-1500. For this experimental set-up, the dwell time per pixel was 1000-1500 ms, which resulted in a total data acquisition time of *ca.* 20 minutes per spheroid section. 9AA was used as a matrix as it is effective in ionizing small molecular weight metabolites including nucleotides and phosphates, which are important in understanding the biology of cancer.

As discussed above, the principal advantage of high spectral resolution MSI is the ability to assign elemental formulae from accurate *m/z* measurements. Thus in an imaging experiment, where the spatial distribution of hundreds to thousands of metabolites are mapped simultaneously, high mass resolution allows assignment of these without the requirement for targeted MS/MS approaches.[25] Figure 1 highlights the differences in the profile mass spectra produced from areas across the diameter of the spheroid (in this case,

the central and outer regions). By inspection of an exported representative pixel from the outer and centre region, it is clear that spectra from the spheroid are highly complex, and significant differences in the profile mass spectra are apparent in two regions (Figure 1A). Across the entire spectrum, formulae were assigned to each peak with sub-ppm error and database searches offered tentative metabolite identifications. A narrow region of each spectrum is shown in Figure 1B, highlighting the variation in abundance of species between the outer and centre region of the spheroid. The intensity of these peaks is consistent across the spheroid as shown by the ion density maps (Figure 1C).

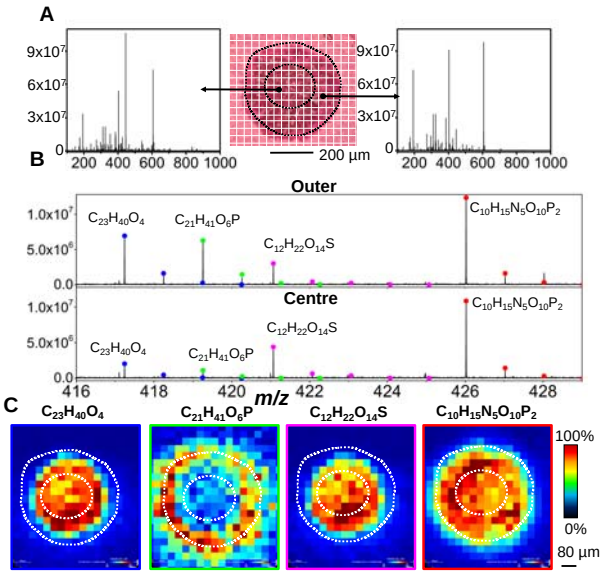

Figure 1. (A) A representative H&E stained section of the MCF-7 spheroids used in this study. A FT-ICR mass spectrum from a representative pixel in the outer and centre regions of the MCF-7 spheroid is shown. (B) Representative pixels from the (top) outer and (bottom) centre region of an MCF-7 spheroid imaged at 50 µm resolution. Using HMDB, each peak could be assigned with sub-ppm error and the relative intensity compared between the regions. The errors identified were 0.0719, 0.3816, 0.2375 and 0.1174 ppm for each assigned formula respectively. (C) The ion density maps for each of the formula assigned are displayed.

MS imaging highlights redox and energy gradients across MTS. During MSI, the signal abundance of an ion irradiated from any point is assumed to be proportional to the concentration of the targeted analyte. However this view is over simplistic, as the analytes present in different areas of a sample could be ionized to varying extents as a result of ion suppression and sample preparation.[29,30] Alternatively, the proportional abundance of individual ions can be used to compare how their ratios change in different locations across the tissue.[31] Using this approach, we can use a targeted method and compare the distributions of known metabolites within MTS (supporting information, Table S2). Initially we chose to analyze the distributions of oxidized/reduced glutathione and high energy adenosine phosphates as these are thought to be affected by the nutrient and oxygen gradients within MTS.[32]

An increased distribution of adenosine triphosphate (ATP) in the outer region of the spheroid indicates a decreasing oxygen gradient through the spheroid. Almost every cellular process requires energy, converting ATP to adenosine diphosphate (ADP) and phosphate. As a result, one of the fundamental parameters that all living cells must maintain is a high ratio of ATP to ADP. At equilibrium, the ratio for ATP:ADP under intracellular conditions is around 10^{-7}:1. However, living cells maintain this ratio around 10:1; 10^8 orders of magnitude away from equilibrium.[33] This ratio is a central control parameter of intracellular energy metabolism that determines the free-energy change for ATP hydrolysis and therefore the driving force for many reactions.[34] For example, in glucose metabolism, the ATP:ADP ratio determines whether the reaction flux through phosphoglycerate kinase is in the glycolytic or gluconeogenic direction.[34] If mitochondrial ATP synthesis becomes compromised when the cell is under stress, such as during hypoxia, the ATP:ADP ratio drops dramatically. This results in stimulation of glycolysis to generate ATP anaerobically. The ATP yield per mole of glucose is much lower for glycolysis compared to mitochondrial oxidative phosphorylation (2 moles of ATP vs. ~35 moles of ATP per mole of glucose, respectively).[35] Interestingly, the total ATP:ADP ratio in spheroids is thought to be reduced compared to monolayer cell culture.[36] Furthermore, as spheroids age and increase in size, the rate of glycolysis increases.[36] This suggests that whilst monolayer and small spheroids rely primarily on oxidative phosphorylation for energy production, larger spheroid's energy demand is predominantly supported by the glycolytic pathway.[36] As a result, the ability to observe changes in the ATP:ADP ratio can be used to visualize energy changes in cells.[37]

Ions corresponding to ATP, ADP and AMP are all observed in our MSI data of MCF-7 spheroids, and all three biomolecules display consistent gradients across multiple separately imaged spheroids (supporting information, Figure S2). Importantly, the high spectral resolution obtainable by FT-ICR enables the observation of isotopic fine structure (IFS) of the first isotope peak for ATP, ADP and AMP (i.e. the mass discrepancy between ^{13}C and ^{15}N) to increase the confidence of the formula assignment (supporting information, Figure S3). The distributions of the $[M-H]^-$ *m/z* value of ATP (*m/z* 505.9885) localized distinctly towards the outer region of the MCF-7 spheroid with 0.140 ppm error (Figure 2). In contrast, ADP (*m/z* 426.0221) and adenosine monophosphate (AMP) (*m/z* 346.0558) are more uniformly localized across the spheroid with 0.167 and 0.179 ppm errors respectively. The observed ratio of ion abundance for ATP and ADP shows that, although ADP has a higher abundance in both the outer and centre of the spheroid, there is a marked decrease in the ATP:ADP ion ratio in the center (Figure 2C). This observation suggests that that there is a lower rate of ATP production relative to dephosphorylation in this central region of the spheroid, and the cellular environment is energy depleted, and potentially hypoxic compared to the outer region of the spheroid.

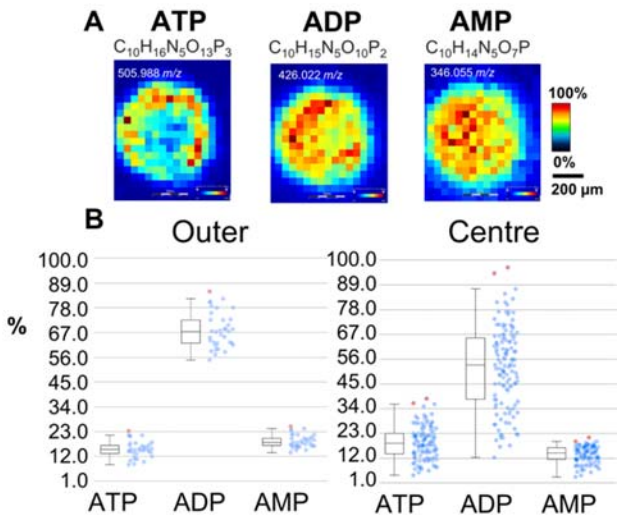

Figure 2. (A) Ion density map of ATP, ADP and AMP across an MCF-7 spheroid imaged at 50 µm resolution using the FT-ICR MSI and 9AA matrix application. (B) Box and whisker plot showing the intensity of the peak for each pixel in the allocated outer and centre regions.

An increased ratio of glutathione disulfide to glutathione is indicative of hypoxic environment in the central region of the spheroid. The tripeptide glutathione (GSH) plays an important role in maintaining the cellular redox homeostasis through oxidation of its sulfhydryl group to form glutathione disulfide (GSSG).[38] The overall concentration of GSH varies between organisms, however it exists in *vivo* predominantly in the reduced form to maintain the GSH:GSSG ratio and avert oxidative stress and apoptosis.[39] Under oxidative stress GSH is oxidized, resulting in an intracellular redox imbalance reflected by a decreased GSH:GSSG ratio.[40] Thus the ratio of GSH:GSSG has been proposed to be a marker for the oxidative nature of the cellular environment and a potential indicator of oxidative stress.

The distributions of the $[M-H]^-$ *m/z* values of GSSG (*m/z* 611.1447) and GSH (*m/z* 306.0765) were imaged within the MCF-7 spheroid with 0.294 ppm and 0.289 ppm errors respectively (Figure 3). Overall, both GSSG and GSH increase in intensity towards the centre of the spheroid (Figure 3A). However, the observed ratio of ion abundance for the GSH:GSSG ions differs in the two regions and a clear decrease in this ratio was observed in the inner region. (Figure 3B). This observation was consistent across biological replicates (supporting information, Figures S4 and S5) and the average GSH:GSSG abundance ratios were determined to be 1.01 (σ=0.31) and 0.78 (σ=0.08) for the outer and central regions respectively (N=6). These findings suggest that the oxidized form is present in a higher relative abundance compared to the reduced form in the central region of the spheroid, consistent with greater oxidative stress experienced in this central region.

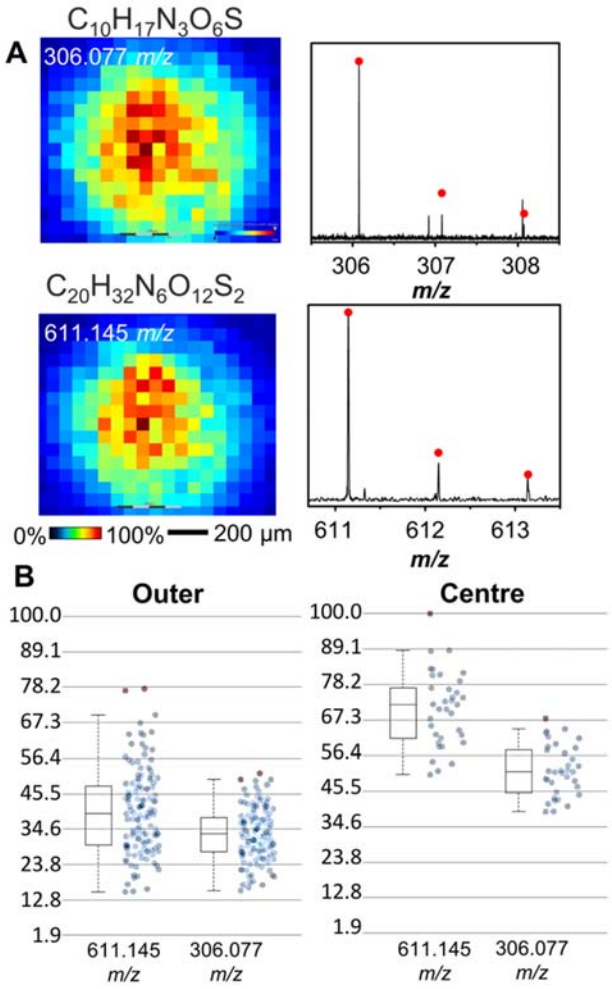

Figure 3. (A) Ion density map of oxidized (*m/z* 611.1447) and reduced (*m/z* 306.0765) glutathione with overlaid spectra showing with 0.294 ppm and 0.289 ppm errors respectively. (B) The box and whisker plots correspond to the intensity of the *m/z* value for each pixel allocated to the outer and center region. Note that the intensity of the oxidized form is greater relative to the reduced form in the center region.

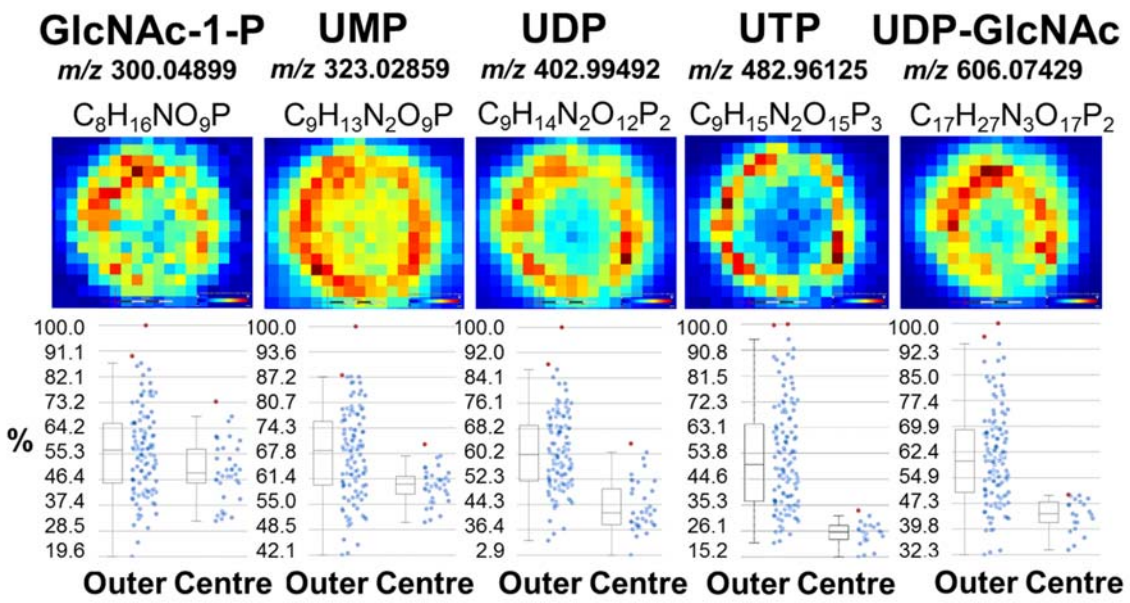

Figure 4. Discriminatory analysis for the identified five outer discriminatory molecules. Formula were assigned with a sub-ppm error and their ion density map, box and whisker plot of the intensities are shown for each formula identified. **GlcNAc-1-P** N-acetyl glucosamine-1-phosphate; **UMP** uridine monophosphate; **UDP** uridine diphosphate; **UTP** uridine triphosphate; **UDP-GlcNAc** uridine diphosphate-N-acetyl glucosamine .

Discriminatory analysis was performed to identify metabolites that are affected most by the hypoxia-induced oxidative stress produced across the spheroid's diameter. For this analysis, two regions were defined within a spheroid as the 'outer' and 'center' based on 50 % of the radius (supporting information, Figure S6). For each *m/z* value the area under the receiver operating characteristic curve (AUC of ROC) was determined and the top five discriminatory metabolites in each region were tentatively identified based on their *m/z* using HMDB. More detailed information for each analysis is available in the supporting information (supporting information, Tables S3 and S4).

High energy uridine phosphates are localized to areas of high oxygen availability. The five molecules that discriminated most strongly towards the outer region were identified using the HMDB with a sub-1 ppm error (Figure 4). Remarkably, all five of the discriminatory molecules were identified as uridine phosphates based on their *m/z* and isotopic fine structure. This is in agreement with recent findings that hypoxia is associated with decreased abundance of uridine nucleosides.[41,42]

In our data, uridine triphosphate (UTP) (AUC = 0.960), uridine diphosphate (UDP) (AUC = 0.992) and UDP-N-acetyl hexose isomers, such as UDP-N-acetylglucosamine (UDP-GlcNAc) (AUC = 0.887) display gradients across the diameter of a spheroid. These distributions were reproducible across multiple biological replicates (supporting information, Figure S7) These metabolites play central roles in the hexosamine biosynthetic pathway (HBP), from which the high energy end product UDP-GlcNAc is catabolized from glucose, glutamine, acetyl-CoA and UTP.[43] Subsequently, UDP-GlcNAc plays an important role in proliferation by contributing to the synthesis of glycosaminoglycans, proteoglycans, and glycolipids that regulate cell signalling and enzyme activity in primary metabolism.[44,45]

It is thought that under conditions of energetic surplus, up to 10% of glycolytic flux can be redirected into the HBP to produce UDP-GlcNAc. In contrast, insufficient oxygen inhibits the HBP and redirects glucose through glycolysis to produce ATP as an energy source.[46,47] This is supported by our findings that in the central hypoxic region of the spheroid there are marked decreased levels of HBP intermediates. In addition, we also observed upregulation of assigned glycolysis intermediates in the centre of the spheroid. This included $C_6H_{13}O_9P$ (*m/z* 259.0224) corresponding to hexose-monophosphates (e.g. glucose-6-phosphate (G-6-P), galactose-6-phosphate and fructose-6-phosphate (F-6-P)) and fructose-1,6-bisphosphate (F-1,6-BisP) (*m/z* 338.9888) (Figure 5). The cleavage of F-1,6-BisP during the next steps of glycolysis produces dihydroxyacetone phosphate (DHAP) and glycerol-3-phosphate, whose distributions were not observed.

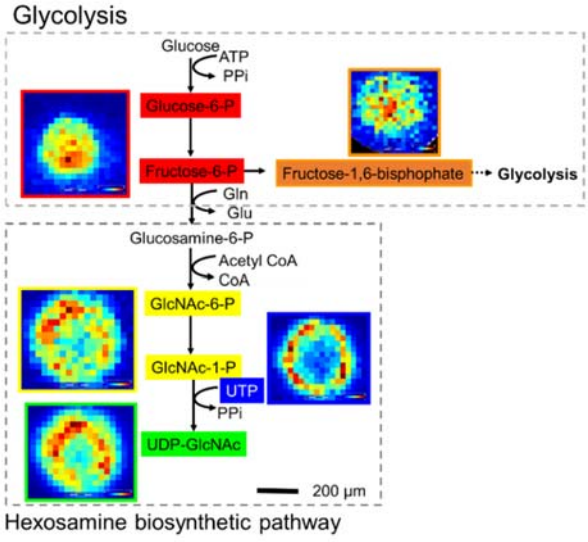

Figure 5. The elemental formula of the metabolites assigned can be mapped onto the hexosamine biosynthetic pathway (HBP). Note how the HBP is upregulated in the outer region, whereas glycolysis

intermediates are upregulated in the centre region. Glucosamine-6-P was not observed.

High energy cytidine phosphates localize in areas of low oxygen availability. The five molecules that discriminated most strongly towards the centre region were also identified using the HMDB with sub-1 ppm error. Four of these are related metabolites and all contain cytidine, including cytidine diphosphate (CDP) (AUC = 0.967), cytidine monophosphate (CMP) (AUC = 0.978), CDP- ethanolamine (AUC = 0.979), and cytidine-2', 3'-cyclic phosphate (AUC = 0.950) (Figure 6). These distributions were reproducible across 6 biological replicates (supporting information, Figure S8). Cytidine and uridine have a mass difference of 0.9840 Da, (UDP: $[M-H]^-$ *m/z* 323.02859; CDP: $[M-H]^-$ *m/z* 322.0446). Therefore, we note that the high spectral resolution offered by FT-ICR allows the resolution of the monoisotopic peak of UDP to the first isotope of CDP with ease (Supporting information, Figure S9).

High-energy cytidine phosphates are utilized in the post-translational modification of glycoproteins and glycosylation of glycolipids with N-acetylneuraminic acid (NeuNAc), the end-product of the sialic acid pathway (Figure 7). Interestingly, there is evidence that cancer cells present elevated levels of neuraminic acid which has been suggested to play an important role in malignancy and the evasion of the immune system.[45] Furthermore, it is thought that hypoxia further increases the expression of intracellular NeuNAc.[48]

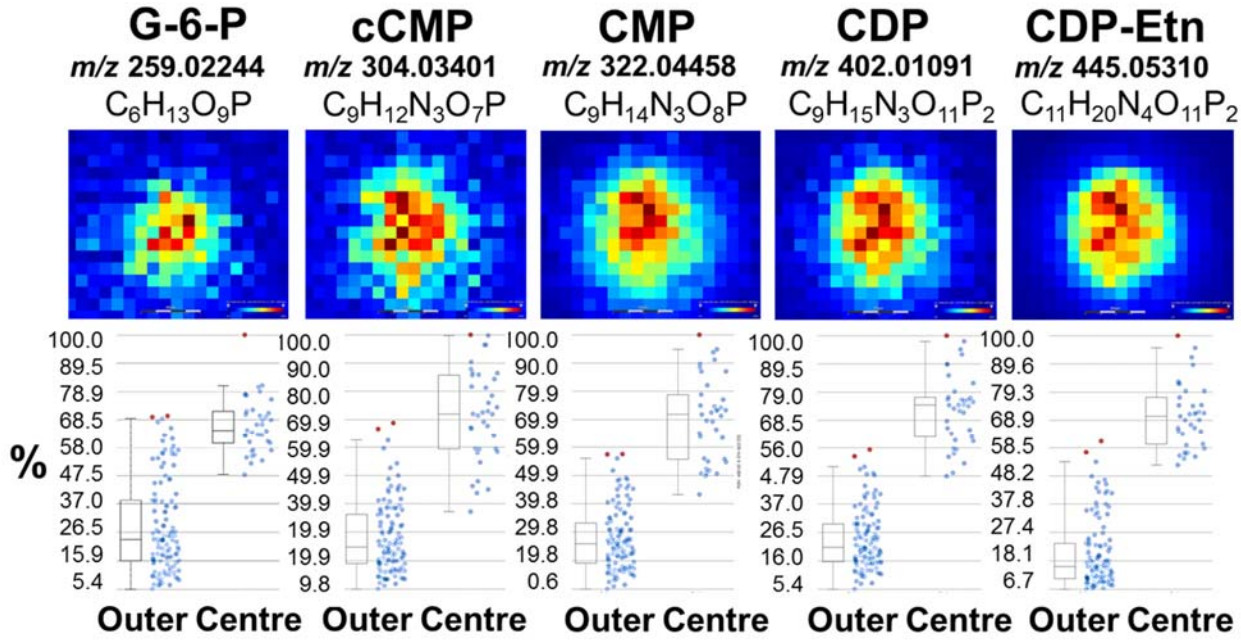

Figure 6. Discriminatory analysis for the identified five centre discriminatory molecules. Formula were assigned with a sub-ppm error and their ion density map (top), and box and whisker plot (bottom) are shown for each formula identified**. G-6-P** Gluocse-6-phosphate ; **cCMP** cytidine-2'3'- cyclic phosphate; **CMP** cytidine monophosphate; **CDP** cytidine diphosphate; F-1-P), **CDP-Etn** cytidine diphosphate ethanolamine.

In addition, the sialic acid pathway and the HBP are closely linked, whereby NeuNAc can be converted to CMP-NeuNAc for use in the sialic pathway, or alternatively isomerized to N-acetylmannosamine (ManNAc) which can be converted back into GlcNAc and salvaged back into the HBP (Figure 7).[47] As shown in our data, the intermediates of both these pathways have distinct distributions in the MTS. As discussed above, high energy uridine phosphates associated with the HBP are localized towards the outer proliferative regions (Figure 5). In contrast, high energy cytidine phosphates distribute towards the oxidative hypoxic conditions of the central region (Figure 7). These distibutions suggest that the microenvironments within MTS display distinct metabolic fluxes in these pathways.

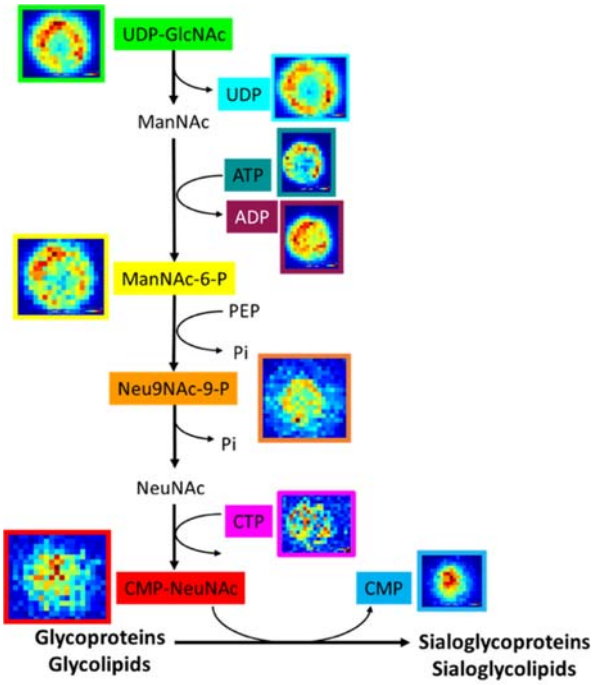

Figure 7**.** Sialic acid pathway. N-acetyl neuraminic acid (sialic acid) is formed by the end product of the hexosamine pathway (HBP). **UDP-GlcNAc** Uridine N-acetylglucosamine; **UDP** Uridine diphosphate; **ATP** adenosine triphosphate; **ADP;** adenosine diphosphate; **ManNAc-6-P** N-acetylmannosamine-6-phosphate; **Neu9NAc-9-P** N-acetylneuraminic acid-9-phosphate; **NeuNAc** N-acetylneuraminic acid; **CMP-NeuAc** cytidine monophosphate N-acetylneuraminic acid; **CMP** cytidine monophosphate.

In the context of cancer biology, the requirement for high energy co-substrates during the synthesis of both CMP-NeuNAc and UDP-GlcNAc as part of glycan production suggests that cancer cells have effective coping mechanisms for maintaining surface sialylation under nutrient deprivation. These metabolic flux-driven changes could contribute to the propensity of a tumor to adapt its metabolism to different environments.

Conclusions

Here we have shown the application of high resolution MSI to determine metabolite distributions within MTS cell culture models. We show that metabolite markers can be used to indicate regions of increased oxidative stress and hypoxia. In addition, we highlight that the information obtained using this approach may be informative for investigating the regional flux through biochemical pathways. We have shown that there is upregulation of metabolic branch pathways such as the HBP in the regions of the spheroid with greater access to oxygen. Conversely, there is greater glycolytic flux within the regions limited by hypoxia. However, the presence of ionization bias enables the comparison of relative intensities, but prevents any definitive quantification of the distributions observed Whilst MSI using FT-ICR provides unparalleled spectral resolution allowing confident elemental assignment, the acquisition time is inherently slow as the high mass resolving power requires long transients to be acquired for each pixel.[23] By increasing the transient recording time, FT-ICR produces an approximately linear improvement for mass resolution.[49] However, given that a typical MS image can consist of tens of thousands of pixels, acquisition time may become a constraining factor. Thus there is in effect a trade-off between spectral resolution and data aquisition time.. However, in comparison to animal tissue samples, the small size of MTS mitigates this disadvantage somewhat, allowing multiple biological replicates to be analyzed on realistic timescales. Therefore, this methodology shows great promise for applications in toxicity studies during drug development, whereby the absorption, distribution and metabolism of the drug could be correlated with its effects on cellular metabolism.

ASSOCIATED CONTENT

Calibration table used for analysis (PDF) Assignments and errors for targeted and untargeted analysis (PDF) H&E stains of sectioned MCF-7 spheroids (PDF) Biological replicates of each metabolite identified for targeted and untargeted analysis (PDF) Fine isotope structure for ATP, ADP and AMP (PDF) Detailed analysis including ROC plots for discriminatory analysis of metabolites for both outer and center regions (PDF). This material is available free of charge via the Internet at http://pubs.acs.org. The MS datasets described in this study are available to download from the Clarke Research Group Data Collection at Edinburgh DataShare (https://datashare.is.ed.ac.uk/handle/10283/760) using the following link: https://doi.org/10.7488/ds/2490.

AUTHOR INFORMATION

Corresponding Author

* Email: dave.clarke@ed.ac.uk Phone: 0131 650 4808
* Email: colin.campbell@ed.ac.uk Phone: 0131 651 3049

Author Contributions

L.H.T. collected the data and wrote the manuscript. G.R.H., C.L.M., C.J.C., R.J.A.G., and D.J.C. all contributed guidance on the manuscript. C.L.M., C.J.C. and D.J.C. planned the experimental work. All authors have given approval to the final version of the manuscript.

ACKNOWLEDGMENT

Funding was provided by AstraZeneca and an EPSRC CASE-studentship to L. H. T.

ABBREVIATIONS

2D, two dimensional; 3D, three dimensional; MTS Multicellular tumor spheroids; PAGE, 2D polyacrylamide gel electrophoresis; LC-MS, liquid chromatography mass spectrometry; SILAC, stable isotope labelling of amino acids in cell culture; MSI, mass spectrometry imaging; MALDI, matrix assisted laser desorption/ionization; ToF, time-of-flight; FT-ICR, Fourier-transform ion cyclotron resonance; SRM, single reaction monitoring; H&E, haematoxylin and eosin; 9AA, 9-aminoacridine; ROC, receiver operating characteristic; AUC, area under the ROC curve; ATP, adenosine triphosphate; ADP, adenosine diphosphate; AMP, adenosine monophosphate; GSH, glutathione; GSSG, glutathione disulfide; ROS, of reactive oxygen species; HIF-1α, hypoxia-inducible factor; UTP, uridine triphosphate; UDP, uridine diphosphate; GlcNAc, N-acetylglucosamine; UDP-GlcNAc, UDP-N-acetylglucosamine; HBP, hexosamine biosynthetic pathway; G-6-P, glucose-6-phosphate; F-6-P, fructose-6-phosphate; F-1,6-BisP, fructose-1,6-bisphosphate; DHAP, dihydroxyacetone phosphate; CDP, cytidine diphosphate; CMP, cytidine monophosphate; CDP-Etn, CDP- ethanolamine; cCMP, cytidine-2', 3'-cyclic phosphate; NeuNAc, N-acetylneuraminic acid; ManNAc, N-acetylmannosamine; DESI, desorption electrospray.

REFERENCES

(1) Breslin, S.; O'Driscoll, L. Three-dimensional cell culture: the missing link in drug discovery. *Drug Discov. Today* **2013**, *18* (5-6), 240–249.

(2) Fennema, E.; Rivron, N.; Rouwkema, J.; van Blitterswijk, C.; De Boer, J. Spheroid culture as a tool for creating 3D complex tissues. *Trends Biotechnol.* **2013**, *31* (2), 108–115.

(3) Liu, X.; Flinders, C.; Mumenthaler, S. M.; Hummon, A. B. MALDI Mass Spectrometry Imaging for Evaluation of Therapeutics in Colorectal Tumor Organoids. *J. Am. Soc. Mass Spectrom.* **2018**, *29*, 516–526.

(4) Kunz-Schughart, L. A.; Kreutz, M.; Knuechel, R. Multicellular spheroids a three-dimensional in vitro culture system to study tumour biology. *Int. J. Exp. Path.* **1998**, *79* (1), 1–23.

(5) Li, H. H.; Hummon, A. B. Imaging Mass Spectrometry of Three-Dimensional Cell Culture Systems. *Anal. Chem.* **2011**, *83* (22), 8794–8801.

(6) Jamieson, L. E.; Camus, V. L.; Bagnaninchi, P. O.; Fisher, K. M.; Stewart, G. D.; Nailon, W. H.; McLlaren, D. B.; Harrison, J.; Campbell, C. J. Targeted SERS nanosensors measure physicochemical gradients and free energy changes in live 3D tumor spheroids, *Nanoscale* **2016**, *37*, 16710–16718.

(7) Pruksakorn, D.; Lirdprapamongkol, K.; Chokchaichamnankit, D.; Subhasitanont, P.; Chiablaem, K.; Svasti, J.; Srisomsap, C. Metabolic alteration of HepG2 in scaffold-based 3-D culture: Proteomic approach. *Proteomics* **2010**, *10* (21), 3896–3904.

(8) Feist, P. E.; Sun, L.; Liu, X.; Dovichi, N. J.; Hummon, A. B. Bottom-up proteomic analysis of single HCT 116 colon carcinoma multicellular spheroids. *Rapid Commun. Mass Spectrom.* **2015**, *29* (7), 654–658.

(9) Yue, X.; Lukowski, J. K.; Weaver, E. M.; Skube, S. B.; Hummon, A. B. Quantitative Proteomic and Phosphoproteomic Comparison of 2D and 3D Colon Cancer Cell Culture Models. *J. Proteome Res.* **2016**, *15* (12), 4265–4276.

(10) Feist, P. E.; Sidoli, S.; Liu, X.; Schroll, M. M.; Rahmy, S.; Fujiwara, R.; Garcia, B. A.; Hummon, A. B. Multicellular Tumor Spheroids Combined with Mass Spectrometric Histone Analysis to Evaluate Epigenetic Drugs *Anal. Chem.* **2017**, *89* (5), 2773–2781.

(11) Ahlf, D. R.; Masyuko, R. N.; Hummon, A. B.; Bohn, P. W. Correlated mass spectrometry imaging and confocal Raman microscopy for studies of three-dimensional cell culture sections. *Analyst* **2014**, *139* (18), 4578.

(12) Goodwin, R. J. A. Sample preparation for mass spectrometry imaging: small mistakes can lead to big consequences. *J. Proteomics* **2012**, *75* (16), 4893–4911.

(13) Spengler, B. Mass Spectrometry Imaging of Biomolecular Information. *Anal. Chem.* **2015**, *87*, 64–82.

(14) Chaurand, P.; Schwartz, S. A.; Billheimer, D.; Xu, B. J.; Crecelius, A.; Caprioli, R. M. Profiling and imaging proteins in tissue sections by mass spectrometry. *Anal. Chem.* **2004**, *76*, 1145–1155.

(15) Weaver, E. M.; Hummon, A. B. Imaging mass spectrometry: From tissue sections to cell cultures. *Adv. Drug Deliv. Rev.* **2013**, *65* (8), 1039–1055.

(16) Stoeckli, M.; Chaurand, P.; Hallahan, D. E.; Caprioli, R. M. Profiling and imaging proteins in tissue sections by mass spectrometry. *Nat. Med.* **2001**, *7* (4), 493–496.

(17) Chaurand, P.; Schwartz, S. A.; Reyzer, M. L.; Caprioli, R. M. Imaging mass spectrometry: principles and potentials. *Toxicol. Pathol.* **2005**, *33* (1), 92–101.

(18) Hiraide, T.; Ikegami, K.; Sakaguchi, T.; Morita, Y.; Hayasaka, T.; Masaki, N.; Waki, M.; Sugiyama, E.; Shinriki, S.; Takeda, M.; Shibasaki, Y.; Miyazaki, S.; Kikuchi, H.; Okuyama, H.; Inoue, M.; Setou, M.; Konno, H. Accumulation of arachidonic acid-containing phosphatidylinositol at the outer edge of colorectal cancer. *Sci. Rep.* **2016**, *6*, 1–11.

(19) Liu, X.; Weaver, E. M.; Hummon, A. B. Evaluation of therapeutics in three-dimensional cell culture systems by MALDI imaging mass spectrometry. *Anal. Chem.* **2013**, *85* (13), 6295–6302.

(20) Liu, X.; Hummon, A. B. Chemical Imaging of Platinum-Based Drugs and their Metabolites *Sci. Rep.* **2016**, *6*, 1–10.

(21) Niehoff, A. C.; Grünebaum, J.; Moosmann, A.; Mulac, D.; Söbbing, J.; Niehaus, R.; Buchholz, R.; Kröger, S.; Wiehe, A.; Wagner, S.; Sperling, M.; von Briesen, H.; Langer, K.; Karst, U. Quantitative bioimaging of platinum group elements in tumor spheroids. *Anal. Chim. Acta* **2016**, *938*, 106–113.

(22) Acland, M.; Mittal, P.; Lokman, N. A.; Klingler-Hoffmann, M.; Oehler, M. K.; Hoffmann, P. Mass Spectrometry Analyses of Multicellular Tumor Spheroids. Proteomics - *Clin. Appl.* **2018**, *75*, 5077-5092.

(23) Jungmann, J. H.; Heeren, R. M. A. Emerging technologies in mass spectrometry imaging *J. Proteomics* **2012**, *75* (16), 5077–5092.

(24) Cornett, D. S.; Frappier, S. L.; Caprioli, R. M. MALDI-FTICR imaging mass spectrometry of drugs and metabolites in tissue. *Anal. Chem.* **2008**, *80* (14), 5648–5653.

(25) Dilillo, M.; Ait-Belkacem, R.; Esteve, C.; Pellegrini, D.; Nicolardi, S.; Costa, M.; Vannini, E.; De Graaf, E. L.; Caleo, M.; McDonnell, L. A. Ultra-High Mass Resolution MALDI Imaging Mass Spectrometry of Proteins and Metabolites in a Mouse Model of Glioblastoma. *Sci. Rep.* **2017**, *7* (1), 1–11.

(26) Buck, A.; Ly, A.; Balluff, B.; Sun, N.; Gorzolka, K.; Feuchtinger, A.; Janssen, K.; Kuppen, P. J. K.; Velde, C. J. H. Van De; Weirich, G.; Erlmeier, F.; Langer, R.; Zitzelsberger, H.; Aichler, M.; Walch, A. High-resolution MALDI-FT-ICR MS imaging for the analysis of metabolites from formalin-fixed, paraffin-embedded clinical tissue samples. *J. Pathol.* **2015**, *237*, 123–132.

(27) Prentice, B. M.; Chumbley, C. W.; Caprioli, R. M. Absolute Quantification of Rifampicin by MALDI Imaging Mass Spectrometry Using Multiple TOF/TOF Events in a Single Laser Shot. *J. Mass Spectrom.* **2016**, *50* (4), 703–710.

(28) Tucker, L. H.; Conde-González, A.; Cobice, D.; Hamm, G. R.; Goodwin, R. J. A.; Campbell, C. J.; Clarke, D. J.; Mackay, C. L. MALDI Matrix Application Utilizing a Modified 3D Printer for Accessible High Resolution Mass Spectrometry Imaging. *Anal. Chem.* **2018**, *90* (15), 8742–8749.

(29) Heeren, R. M. A.; Kükrer-Kaletas, B.; Taban, I. M.; MacAleese, L.; McDonnell, L. A. Quality of surface: The influence of sample preparation on MS-based biomolecular tissue imaging with MALDI-MS and (ME-)SIMS. *Appl. Surf. Sci.* **2008**, *255* (4), 1289–1297.

(30) Taylor, A. J.; Dexter, A.; Bunch, J. Exploring Ion Suppression in Mass Spectrometry Imaging of a Heterogeneous Tissue. *Anal. Chem.* **2018**, *90* (9), 5637–5645.

(31) Chughtai, K.; Heeren, R. M. Aa. Mass spectrometric imaging for biomedical tissue analysis. *Chem. Rev.* **2010**, *110* (5), 3237–3277.

(32) Jamieson, L. E.; Harrison, D. J.; Campbell, C. J. Chemical analysis of multicellular tumour spheroids. *Analyst* **2015**, *140*, 3910–3920.

(33) Hardie, D. G.; Scott, J. W.; Pan, D. A.; Hudson, E. R. Management of cellular energy by the AMP-activated protein kinase system. *FEBS Lett.* **2003**, *546* (1), 113–120.

(34) Veech, R. L.; Lawson, J. W.; Cornell, N. W.; Krebs, H. A. Cytosolic Phosphorylation Potential. *J. Biol. Chem.* **1979**, *254* (14), 6538–6547.

(35) Maldonado, E. N.; Lemasters, J. J. ATP/ADP ratio, the missed connection between mitochondria and the Warburg effect. *Mitochondrion* **2014**, *19* (1), 78–84.

(36) Rodriguez-Enriquez, S.; Gallardo-perez, J. C.; Avilrs-Salas, A.; Marin-Hernandez, A.; Carreno-Fuentes, L.; Maldonado-Laguna, V.; Moreno-Sanchez, R. A Krebs Cytosolic Phosphorylation Potential. *J. Cell Physiol* **2008**, *216*, 189–197.

(37) Tantama, M.; Martínez-François, J. R.; Mongeon, R.; Yellen, G. Imaging energy status in live cells with a fluorescent biosensor of the intracellular ATP-to-ADP ratio. *Nat. Commun.* **2013**, *4*, 1-13.

(38) Balendiran, G. K.; Dabur, R.; Fraser, D. The role of glutathione in cancer. *Cell Biochem. Funct.* **2004**, *22* (1), 343–352.

(39) Deponte, M. The Incomplete Glutathione Puzzle: Just Guessing at Numbers and Figures? *Antioxid. Redox Signal* **2017**, *27* (15), 1130–1161

(40) Circu, M. L.; Yee Aw, T. Glutathione and modulation of cell apoptosis. *Biochem. Biophys. Acta.* **2012**, *10* (1823), 1767–1777.

(41) Shirato, K.; Nakajima, K.; Korekane, H.; Shinji Takamatsu, Congxiao Gao, T. A.; Ohtsubo, K.; Taniguchi, N. Hypoxic regulation of glycosylation via the N-acetylglucosamine cycle. *J. Clin. Biochem.* **2011**, *48* (1), 20–25.

(42) Nagana Gowda, G. A.; Barding, G. A.; Dai, J.; Gu, H.; Margineantu, D. H.; Hockenbery, D. M.; Raftery, D. A Metabolomics Study of BPTES Altered Metabolism in Human Breast Cancer Cell Lines. *Front. Mol. Biosci.* **2018**, *49* (5), 1-13.

(43) Ruan, H. Bin; Singh, J. P.; Li, M. D.; Wu, J.; Yang, X. Cracking the O-GlcNAc code in metabolism. *Trends Endocrinol. Metab.* **2013**, *24* (6), 301–309

(44) Clark, P. M.; Dweck, J. F.; Mason, D. E.; Hart, C. R.; Buck, S. B.; Peters, E. C.; Agnew, B. J.; Hsieh-Wilson, L. C.). Direct In-Gel Fluorescence Detection and Cellular Imaging of O -GlcNAc-Modified Proteins. *J. Am. Chem. Soc.* **2008**, *130* (35), 11576–11577.

(45) Pearce, O. M. T.; Läubli, H. Sialic acids in cancer biology and immunity. *Glycobiology* **2016**, *26* (2), 111–128.

(46) Ma, Z.; Vosseller, K. O-GlcNAc in cancer biology. *Amino Acids* **2013**, *45* (4), 719–733.

(47) Badr, H. A.; Alsadek, D. M. M.; Mathew, M. P.; Li, C.; Djansugurova, L. B.; Yarema, K. J. Biomaterials Nutrient-deprived cancer cells preferentially use sialic acid to maintain cell surface glycosylation. *Biomaterials* **2015**, *70*, 23–36

(48) Go, S.; Sato, C.; Yin, J.; Kannagi, R.; Kitajima, K. Hypoxia-enhanced expression of free deaminoneuraminic acid in human cancer cells. *Biochem. Biophys. Res. Commun.* **2007**, *357*, 537–542.

(49) Hendrickson, C. L.; Quinn, J. P.; Kaiser, N. K.; Smith, D. F.; Blakney, G. T.; Chen, T.; Marshall, A. G.; Weisbrod, C. R.; Beu, S. C. 21 Tesla Fourier Transform Ion Cyclotron Resonance Mass Spectrometer: A National Resource for Ultrahigh Resolution Mass Analysis. *J. Am. Soc. mass Spectrom.* **2015**, *26* (9), 1626–1632.

TOC graphical abstract